Geochemistry, Geophysics, Geosystems

RESEARCH ARTICLE
10.1029/2019GC008309

Special Section:
Magmatic and volcanic processes in continental rifts

Pinpointing Deep Geothermal Upflow in Zones of Complex Tectono-Volcanic Degassing: New Insights from Aluto Volcano, Main Ethiopian Rift

E. Jolie[1,2], W. Hutchison[3], D.L. Driba[1,4], A. Jentsch[1], and B. Gizaw[4]

[1]GFZ German Research Centre For Geosciences, Potsdam, Germany, [2]ÍSOR Iceland GeoSurvey, Reykjavík, Iceland, [3]School of Earth and Environmental Sciences, University of St Andrews, St Andrews, UK, [4]GSE Geological Survey of Ethiopia, Addis Abeba, Ethiopia

Abstract Active rifts release large amounts of gases from deep sources to the atmosphere by advection and diffusion processes along permeable fracture zones. The objective of this study is to develop geothermal exploration concepts for areas with little or no hydrothermal surface expressions suitable for fluid sampling and analyses (e.g., hot springs, geysers, and fumaroles). In such areas, soil gas surveys can complement established geophysical and geochemical exploration. We report CO_2, ^{222}Rn (radon), and ^{220}Rn (thoron) emission data and ground temperatures from the Aluto volcanic complex in the Main Ethiopian Rift to improve understanding of tectonic and volcanic controls on the existing geothermal system. This suite of gas emission measurements allows us to identify major, deep-rooted permeable structures with active fluid circulation and identify suitable drilling targets for geothermal production wells on Aluto. We show that significant differences in gas signatures (i.e., efflux and spatial pattern) can be used to identify predominantly volcanically and/or tectonically influenced compartments. Major gas emissions indicate significant fluid circulation at depth, which is typical for magmatic systems. Such high gas emissions have been observed in areas affected by major tectonic structures interacting with magmatic bodies at depth (tectono-volcanic). Predominantly fault-controlled sectors also show hydrothermal fluid circulation, but to a lower extent compared to tectono-volcanic sectors. Within the Aluto volcanic complex, geothermal production wells mainly target such fault-controlled domains, whereas results of the study indicate strongest fluid circulation in tectono-volcanic sectors. This result should be considered for the future exploration and development strategy of the site.

Plain Language Summary Active rifts release large amounts of gases from deep sources to the atmosphere along permeable fracture zones. We report CO_2, ^{222}Rn (radon), and ^{220}Rn (thoron) emission data and ground temperatures from the Aluto volcanic complex in the Main Ethiopian Rift. Results help to improve understanding of tectonic and volcanic controls on the existing geothermal system and are useful to identify suitable drilling targets for geothermal production wells. Variations in gas emissions also allow mapping of permeable structures, even in areas where faults are not obvious. We show that significant differences in gas signatures (i.e., flow rates and spatial pattern) can be used to identify predominantly volcanically and/or tectonically influenced domains. Emissions increase toward the volcanic center implying a deep degassing magmatic body.

Key Points:
- First complete set of CO_2-^{222}Rn-^{220}Rn gas emission data from the Main Ethiopian Rift is reported
- Volatile emissions focus along volcanic and tectonic structures and allow mapping of deep gas sources across the Aluto volcano, Ethiopia
- Emissions increase toward the volcanic centre, implying a degassing magmatic body

Supporting Information:
- Supporting Information S1
- Figure S1
- Figure S2
- Figure S3
- Figure S4

Correspondence to:
E. Jolie,
jolie@gfz-potsdam.de

Citation:
Jolie, E., Hutchison, W., Driba, D. L., Jentsch, A., & Gizaw, B. (2019). Pinpointing deep geothermal upflow in zones of complex tectono-Volcanic degassing: New insights from Aluto volcano, Main Ethiopian Rift. *Geochemistry, Geophysics, Geosystems*, *20*, 4146–4161. https://doi.org/10.1029/2019GC008309

Received 4 MAR 2019
Accepted 17 JUL 2019
Accepted article online 27 JUL 2019
Published online 21 AUG 2019

1. Introduction

The East African Rift System has numerous high-temperature geothermal fields, which offer huge potential for power generation and opportunities for economic development; however, the heterogeneity and complexity of the highly fractured geothermal reservoirs pose major difficulties for their exploration (Younger, 2014). Conventional geophysical and geochemical exploration technologies are useful to prove a resource and understand the large-scale architecture of geothermal systems but do not pinpoint preferential locations for targeting expensive production wells into most permeable pathways. Additionally, geophysical data (e.g., resistivity data) often cannot distinguish active from paleo-hydrothermal activity as the resistivity structure will be preserved in the subsurface, even if systems are cooling (Bibby et al., 1992).

For a successful exploration strategy in these environments, information on the system's current activity and fault permeability (e.g., upflows and outflows) is required at a high spatial resolution. The best geochemical

approach for obtaining such high spatial resolution observations are soil gas surveys (e.g., CO_2, ^{222}Rn, and ^{220}Rn), which help to identify the most permeable structures with highest hydrothermal fluid flow (Jolie, Klinkmueller, et al., 2015; Neri et al., 2016). In this paper we prove the suitability of these techniques for geothermal exploration projects.

Major faults in the East African Rift System are controlled by tectonic and volcanic mechanisms. Surface gas release and hydrothermal fluid circulation in active rift systems not only are related to its volcanic heat source but also reflect local and regional tectonic controls in the subsurface (Brune et al., 2017; Goerner et al., 2009; Jolie et al., 2016). Increased degassing along fracture zones outlines deep-rooted permeable segments of active faults and points to major upflow and outflow zones of hydrothermal fluids. Depth of faults is at least 5 km, but no distinct structure could be identified below 8 km based on Magnetotelluric (MT) studies by Samrock et al. (2015). In Tule Moye, a comparable site to Aluto, faults channel magmatic fluids from a depth of ~14 km to the surface (Samrock et al., 2018). Fault segments with strong gas emissions are characterized by increased slip and dilation tendencies (Jolie, Moeck, et al., 2015; Jolie et al., 2016). Analyses of a variety of soil gases have proven their suitability for assessing the tectonic and volcanic controls on geothermal systems (Hunt et al., 2017; Jolie, Klinkmueller, et al., 2015; Jolie et al., 2016; Lee et al., 2016). These gases provide vital information for the exploration of geothermal fields and help in targeting wells in the most permeable structures with the greatest flow rates of high-temperature hydrothermal fluids. Soil gas surveys do not require heavy equipment and can be performed in a relatively short time even in some of the most difficult terrain, where other technologies are limited. Many techniques even allow in situ analysis in the field (e.g., accumulation chamber method, alpha spectroscopy, and gas chromatography), which gives much flexibility in the planning of field campaigns (Jolie, Klinkmueller, et al., 2015).

Aluto offers an ideal location to address some of these issues and understand the architecture of a rift-related alkaline, fault-controlled geothermal system. The volcanic complex has been a target for geothermal exploration and exploitation for several decades (Gebregzabher, 1986; Gianelli & Teklemariam, 1993; Gizaw, 1993; Hochstein et al., 2017; Teklemariam et al., 1996; Valori et al., 1992) as well as recent geological, geochemical, and geophysical investigations (Biggs et al., 2011; Braddock et al., 2017; Hutchison et al., 2015; Hutchison, Biggs, et al., 2016, Hutchison, Fusillo, et al., 2016, Hutchison, Pyle, et al., 2016; Iddon et al., 2018; Nowacki et al., 2018; Saibi et al., 2012; Samrock et al., 2015; Wilks et al., 2017). Although Aluto is wellstudied compared to many of Ethiopia's geothermal prospects, major uncertainties remain about how geothermal fluids are distributed in the subsurface and how they ascend along the mapped fault zones. Answering these questions has implications for understanding Aluto's geothermal system and for characterizing the fault network that might be exploited by future dike intrusions and volcanic events (Hutchison et al., 2015); more generally, it can provide important lessons on how to exploit the complex, highly-fractured alkaline geothermal systems that typify the East African Rift System.

In this study, we show the results of a multi-method approach that focuses on the identification and characterization of degassing fluids that ascend from a magmatic system along tectonic faults (tectono-volcanic interaction). Tectono-volcanic interactions have an effect on soil degassing within the Aluto volcanic complex and result in more intense gas emissions. Our approach consists of a combination of systematic alpha-spectroscopic measurements as well as CO_2 efflux measurements based on an area-wide, regular grid (Jolie, Klinkmueller, et al., 2015; Jolie et al., 2016). Results illustrate that substantial information on permeable subsurface structures and lateral outflows can be obtained by the analysis of surface degassing. This adds more details to the results of conventional structural mapping at the surface, which is often limited in particular in areas with fast geomorphological changes due to strong erosional activity. Soil gas surveys provide useful solutions for a comprehensive analysis of geothermal systems and the identification of suitable areas for geothermal development.

2. Geological Setting

2.1. Regional Geology-The Main Ethiopian Rift

The ~600-km-long Main Ethiopian Rift (MER) is an actively extending magmatic rift that forms the northernmost segment of the East African Rift System (Corti, 2009). The MER shows clear along-axis variations in rift morphology (Molin & Corti, 2015), tectonics (Agostini et al., 2011), and crustal structure (Keir et al., 2015; Maguire et al., 2006) and is usually divided into northern, central, and southern sectors (Figure 1a).

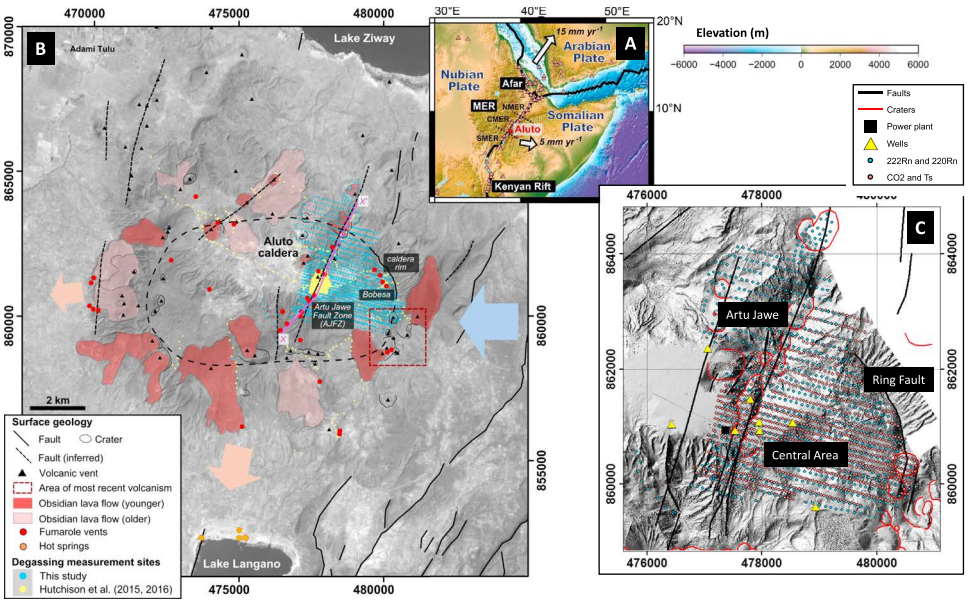

Figure 1. (a) Regional topographic map. The black lines represent major plate boundaries, while pink triangles mark all Holocene volcanoes (after Siebert & Simkin, 2002). The Main Ethiopian Rift (MER) is divided into northern (NMER), central (CMER), and southern (SMER) segments. Aluto volcano, the focus of this study, is located in the CMER and is shown in red. White arrows show current extension vectors relative to a fixed Nubian Plate (after Saria et al., 2014). In (b), a detailed map of the Aluto volcanic complex with a summary of the geology, hydrothermal manifestations, and degassing studies is shown (coordinate system WGS 1984 UTM Zone 37N). The latest version of the geological map of Aluto is available in Hutchison, Pyle, et al. (2016). The large blue arrow shows the presumed inflow of cool groundwater to the geothermal reservoir (after Braddock et al., 2017; Darling et al., 1996), while the smaller orange arrows show the shallow outflow of hot geothermal fluids that feed fumaroles and hot springs on the West and South of the complex. In (c), a detailed map of the study area including all sampling sites for ^{222}Rn, ^{220}Rn, CO_2, and T_S is shown.

Normal fault scarps are prominent at the surface, and two dominant fault sets have been identified: (1) Mid-Miocene border faults and (2) Quaternary-Recent Wonji faults aligned along the rift axis (Boccaletti et al., 1998; Ebinger & Casey, 2001; Mohr, 1967).

Rift magmatism has led to surface volcanism across the MER and Quaternary-Recent volcanoes are mostly concentrated along the rift axis (Di Paola, 1972). Although the styles and geochemistry of MER volcanism is diverse (Fontijn et al., 2018), the most attractive geothermal prospects are hosted by chemically evolved, silicic shield volcanoes and calderas, for example, Corbetti, Aluto, or Gedemsa (Kebede, 2012; Hutchison, Pyle, et al., 2016; Samrock et al., 2018). Satellite remote sensing surveys (e.g., Biggs et al., 2011; Hutchison, Biggs, et al., 2016; Lloyd et al., 2018) have highlighted episodes of ground deformation at a number of these silicic volcanoes (e.g., Aluto and Corbetti). These observations provide compelling evidence for subsurface fluid movement, although contrasting models have been proposed to explain the causes of deformation, including magmatic intrusions, gas and magmatic fluid pulses, and clay swelling (Hutchison, Biggs, et al., 2016; Samrock et al., 2015). Despite this uncertainty, there is a consistent view that pre-existing structures (both tectonic and volcanic in origin) play an important role in controlling the movement of magma, hydrothermal fluids, and gases at these volcanoes (Goerner et al., 2009; Hutchison et al., 2015; Lloyd et al., 2018).

2.2. Aluto Geology and Geothermal Field

Aluto volcano, the focus of this contribution, is located in the central MER (Hutchison et al., 2015, Hutchison, Biggs, et al., 2016, Hutchison, Fusillo, et al., 2016) and is Ethiopia's only exploited geothermal field (Kebede, 2012). Its geological and eruptive history has been the focus of work by Hutchison et al. (2015), Hutchison, Biggs, et al., (2016), Hutchison, Fusillo, et al., (2016) who have shown that the complex was initially built up as a trachytic shield before undergoing a series of large caldera-forming eruptions between 320 and 300 ka. Since ~60 ka, Aluto has been in a post-caldera phase typified by the eruption of small volume ($<250 \times 10^6$ m^3) pumice cones and obsidian domes across the complex. The key structural feature of Aluto is a NNE-SSW (Wonji-aligned) fault known as the Artu Jawe Fault Zone (AJFZ; Hutchison

et al., 2015), and deep well observations suggest that the AJFZ predates the first eruptions of the silicic complex. Young obsidian lava flows seem to be co-located with this major structure and represent a record of the most active structures across Aluto, which channeled magma during eruptive periods and now channel magmatic gases. The AJFZ together with an elliptical ring fault, assumed to have developed during Aluto's caldera collapse, strongly influences magma ascent and also direct hydrothermal fluids toward the surface. Geothermal surface manifestations (e.g., steam vents, alteration, and warm ground) are widely distributed within the volcanic complex, but strong fumaroles and boiling hot springs only occur outside the complex (Figure 1b).

Aluto's geothermal field has also been the focus of numerous surface and deep well investigations (e.g., Gianelli & Teklemariam, 1993; Gizaw, 1993; Teklemariam et al., 1996). Observations from the wells have been used to infer that the main part of the geothermal reservoir is >2,000 m beneath the surface and is sealed by a sequence of intensely altered basalts and tuffs that form a low-permeability, low-resistivity clay cap at ~500–1,500 m (Samrock et al., 2015). The geothermal fluid appears to be primarily sourced from rainfall on the rift margin (Darling et al., 1996; Rango et al., 2010) rather than the surrounding lakes, and there is good evidence from resistivity soundings for major outflows to the South and West (Hochstein et al., 2017). This and the high temperatures indicated by water chemistry, mineralogy, and downhole temperatures (>300 °C; Gizaw, 1993) all suggest that the AJFZ represents a major upflow zone from the deep geothermal reservoir toward the surface. To date, geothermal production wells only target the AJFZ, specifically its Northern Sector (Figure 1).

Previous studies of Aluto's gas emissions (Hutchison et al., 2015, Hutchison, Biggs, et al., 2016) focused mainly on CO_2 and involved a couple of transects of major structures and a small-scale study of the main AJFZ area (Figure 1). These results supported findings from earlier geothermal investigations that identified the AJFZ as the key structure for fluid upflow and geothermal utilization. Hutchison et al. (2015) also found significant anomalous degassing in other areas of the complex (specifically around the caldera rim and ring fault on the east of the complex, Bobesa; Figure 1). Owing to the limited number of sample sites and the focus on CO_2 data, major uncertainites remain about these degassing regions as well as the upflow along the AJFZ. In particular, it is not clear whether (1) all mapped faults are connected to a deep geothermal reservoir; (2) fluid circulation extends along NNE-striking fault zones beyond the boundaries of Aluto volcanic complex; (3) fault intersections provide enhanced permeability and hence good targets for future exploration; and (4) there is any evidence for lateral fluid outflow. By extensive and systematic soil gas measurements (involving a wide range of parameters, CO_2, ^{222}Rn, and ^{220}Rn), we aim to address these challenges by assessing the variability of gas emissions along fracture zones and identifying further permeable but less prominent or maybe even hidden structures.

3. Methods

A large-scale soil gas survey was performed in May 2016 covering a significant area of the two dominating structures (i.e., Artu Jawe and Ring Fault; Figure 1c) as well as the area in between the two structures (referred to as “Central Area”), building up on previous efforts by Hutchison et al. (2015), Hutchison, Biggs, et al., (2016). A second small-scale survey was performed in early 2017 to extend the survey area to the North and Northwest for a comprehensive understanding of the NNE continuation of the AJFZ and the continuation of the Ring Fault to the West. The NE-SW extension of the study area is 5.7 km with a maximum NW-SE extension of 3.5 km. The following parameters were determined during the field survey-CO_2 efflux by the accumulation chamber method, ^{222}Rn and ^{220}Rn activity concentration by alpha-spectroscopic measurements, and soil temperatures (T_S) at 50 cm depth (Table 1; Fridriksson et al., 2016; Jolie, Klinkmueller, et al., 2015). The accumulation chamber method is a technology where a chamber is placed on the ground and the increasing CO_2 concentration in the chamber is measured (2–3 min) by an infrared gas analyzer (LI-COR 820, accuracy <3% of reading). The increase in CO_2 concentration correlates to the CO_2 efflux at the interface from geosphere to atmosphere. Throughout the survey, we used a WEST Systems Type A accumulation chamber (WEST Systems, 2019). Temperature measurements have been performed using a Greisinger GMH 285-BNC thermometer with Pt1000 sensor in a 620-mm-long stainless steel probe (accuracy ±0.1 K). ^{222}Rn and ^{220}Rn activity concentrations are determined by a radiometric measurement (~15 min), which determines their short-living radon daughter nuclides ^{218}Po and ^{216}Po from soil

Table 1
Summary of All Measured Parameters

Parameter	CO_2 (g·m^{-2}·day^{-1}]	^{222}Rn (kBq·m^{-3})	^{220}Rn (kBq·m^{-3})	T (°C)
Number of samples	1,280	726	721	885
Min	0.9	558	177	18.1
Max	25,084 (DL*)	1,050.7	562.3	95.1
Mean (arithm.)	333.9	36.2	19.6	27.0
Median	61.6	19.8	12.89	23.6
Grid dimension	55 × 100 m 55 × 200 m	100 × 175 m	100 × 175 m	55 × 100 m 55 × 200 m

Note. The maximum encountered CO_2 efflux value was above the detection limit (DL) of the device and therefore set to the maximum measurable CO_2 efflux value.

gas samples collected 1 m below the surface (Jolie, Klinkmueller, et al., 2015) and pumped to the analyzer. Measurements have been performed by a Sarad RTM 1688 and RTM 2200 using a high-voltage measuring chamber with electrostatic precipitation of ionized nuclides on the surface of a 2 cm^2 semiconductor silicon detector (accuracy: 3 counts/min).

3.1. Radon Versus Thoron

Radon (^{222}Rn) and thoron (^{220}Rn) activity concentrations have been used for the assessment of hydrothermal upflow zones in geothermal resources (Jolie, Klinkmueller, et al., 2015). ^{222}Rn activity concentrations above and in the vicinity of hydrothermal upflow zones usually result in increased gas concentrations. In general, measurable activity concentrations of both parameters depend primarily on (1) the depth of the uranium/thorium source in the subsurface, (2) the fluid migration velocity from the subsurface to the surface, and (3) the different decay velocities for ^{222}Rn ($T_{1/2} = 3.8$ days) and ^{220}Rn ($T_{1/2} = 55.6$ s). This means that in areas with fast fluid migration velocities from the geothermal reservoir to the surface ^{220}Rn values can also reach peak values. Assuming that the approximate source for uranium and thorium is at a constant depth level throughout the study area, different fluid migration velocities toward the surface have a strong impact on the ^{222}Rn-^{220}Rn ratios (RTR). In practical terms, it means that multiple RTRs can indicate geothermal upflows from depth, instead of one specific ratio. This requires a careful interpretation. A ^{222}Rn-^{220}Rn plot from the five sectors with the main degassing features allows one to identify major upflow zones. During the migration of fluids to the surface, a lot more ^{220}Rn than ^{222}Rn is lost due to decay as a result of its short half-life of 55.6 s, compared to 3.8 days for ^{222}Rn. This effect causes significantly increased RTRs at medium fluid migration velocity. However, if the transport velocity is high enough, both ^{222}Rn and ^{220}Rn will result in maximum values and consequently intermediate RTRs. Conversely, shallow uranium/thorium sources could also result in increased ^{222}Rn and particularly high ^{220}Rn activity concentrations (low RTRs); however, this would require high-temperature geothermal activity for fluid-rock interaction, which mainly occurs in deep geothermal reservoirs. In that sense, it is possible to differentiate between (1) deep sources/medium upflow velocity (high RTR: 6.7–33), (2) deep sources/fast upflow velocity (intermediate RTR: 1.5–3.9), and (3) shallow sources (low RTR: 0.3–0.7).

3.2. Soil Gas Fingerprint

Fingerprint analyses are widely used in geochemistry, but fingerprints for multi-parameter soil gas datasets are still a novel processing and visualization technique and presented herein for the first time. Soil gas fingerprints give a more comprehensive understanding and classification of the spatial variability of gas emissions by plotting maximum (mean) values of each analyzed parameter from selected compartments of a study area, normalized to the maximum (mean) values observed in the entire study area. These compartments define themselves by particularly high or low soil gas emissions and other geological or hydrological conditions (e.g., terrain, known faults, rivers, and geothermal surface manifestations). In some cases, multiple scenarios for compartments need to be defined and tested for one area. The method allows fast comparison of spatial trends and differences for an unlimited number of parameters. Soil gas fingerprints can be determined for any specific area and aerial extent. Ongoing research activities will further improve this novel approach for a fast assessment and comparison of gas emissions from geothermal fields by including more

parameters. Based on this technique, we aim to differentiate deep from shallow sources, tectonic from volcanic degassing, and other characteristics. In this study, we present a soil gas fingerprint analysis for the key structures.

4. Results

The two major structures in the study area (i.e., Artu Jawe and Ring Fault) have been subdivided (Figures 1c and 2). Artu Jawe Fault was divided into Northern (A1) and Southern AJFZ (A2), where higher gas emissions were determined. Along the Ring Fault, two major degassing clusters were identified; therefore, the area was subdivided into R1 and R2.

4.1. Carbon Dioxide

The CO_2 efflux dataset was statistically separated into different classes based on two major inflection points (CO_2 efflux: 370 and 8,500 $g \cdot m^{-2} \cdot day^{-1}$) in the probability plot (Figure 3). Peak values above 8,500 up to 25,084 $g \cdot m^{-2} \cdot day^{-1}$ (detection limit of the device) are illustrated as points (Figure 2). All values below 350 $g \cdot m^{-2}$ day^{-1} are considered as background efflux. A more detailed assessment of the background population identified two further inflection points at 35 and 160 $g \cdot m^{-2} \cdot day^{-1}$, splitting the background into two distinct populations. Values below 35 $g \cdot m^{-2} \cdot day^{-1}$ are likely to be related to a biogenic source with a mean of 24.9 $g \cdot m^{-2} \cdot day^{-1}$, whereas values up to 160 $g \cdot m^{-2} \cdot day^{-1}$ and above are considered as volcanic background values (Hutchison et al., 2015).

Increased CO_2 efflux values have been measured along Artu Jawe and the Ring Fault, as well as in one well-defined zone in the Central Area (Figure 2). Peak CO_2 efflux values (>8,500 $g \cdot m^{-2} \cdot day^{-1}$) occurred only along the Ring Fault (R1 + R2) and the Southern AJFZ (A2), but not in Northern AJFZ (A1). A strong segmentation of the degassing pattern was observed along the AJFZ, which resembles partly the location and dimension of volcanic eruption craters (A1).

The Central Area (C) hosts two areas with increased degassing rates. A larger anomaly (C1) is located in the Northern part between Artu Jawe and the Ring Fault (referred to as Bobesa) and correlates with increased ^{222}Rn values (without geothermal surface manifestations). Another small anomaly (C2) sits further Southeast where increased T_S and ^{222}Rn were measured (with geothermal surface manifestations).

Existing CO_2 efflux data from 2012 to 2014 and 2016 indicate stable degassing features in space and time for a number of years (Figure 4). This area also represents the transition zone from a structurally dominated segment in the North to a volcanically dominated segment in the South.

4.2. Soil Temperature

Thermal anomalies occur mainly along Artu Jawe (A1 + 2) and the Ring Fault (R1 + 2), plus two areas (C2 + C4) in the eastern Central Area (i.e., steaming ground; Figure 2). C2 seems to be connected to R2. Highest T_S was measured in Southern Artu Jawe and the Ring Fault (R2). Soil temperatures along the Northern AJFZ do not exceed 75 °C. A wide area with slightly increased soil temperatures (up to 32 °C) was identified in the northern part of the study area.

4.3. Radon

The ^{222}Rn activity concentration dataset was statistically separated into different classes based on major and minor inflection points in the probability plot (Figure 3). Peak activity concentrations (>120.4 $kBq \cdot m^{-3}$-mean of PIII) occur along the Southern AJFZ with decreasing values toward the North (Figure 2). Peaks in the northern sector are located within volcanic eruption craters and appear as elongated anomalies. All values below 15.5 $kBq \cdot m^{-3}$ are considered as pure background. Values between 15.5 and 50.1 $kBq \cdot m^{-3}$ are expected to be a mixture of background and peak values.

The map (Figure 2) illustrates a segmented, fault-controlled pattern of increased ^{222}Rn activity concentration along Artu Jawe (mainly characterized by dextral offsets). Compared to CO_2 efflux and T_S, ^{222}Rn gives well-defined anomalies. Two major anomalous, but rather circular areas are located along the Ring Fault (R1 + R2). Three distinct anomalous areas, but with lower magnitudes, were identified in the center (C1 + C2 + C3). The anomaly to the East (C2) coincides with increased soil temperatures. In the northern part of Artu Jawe at the intersection of the Ring Fault and the AJFZ ^{222}Rn values and T_S have only

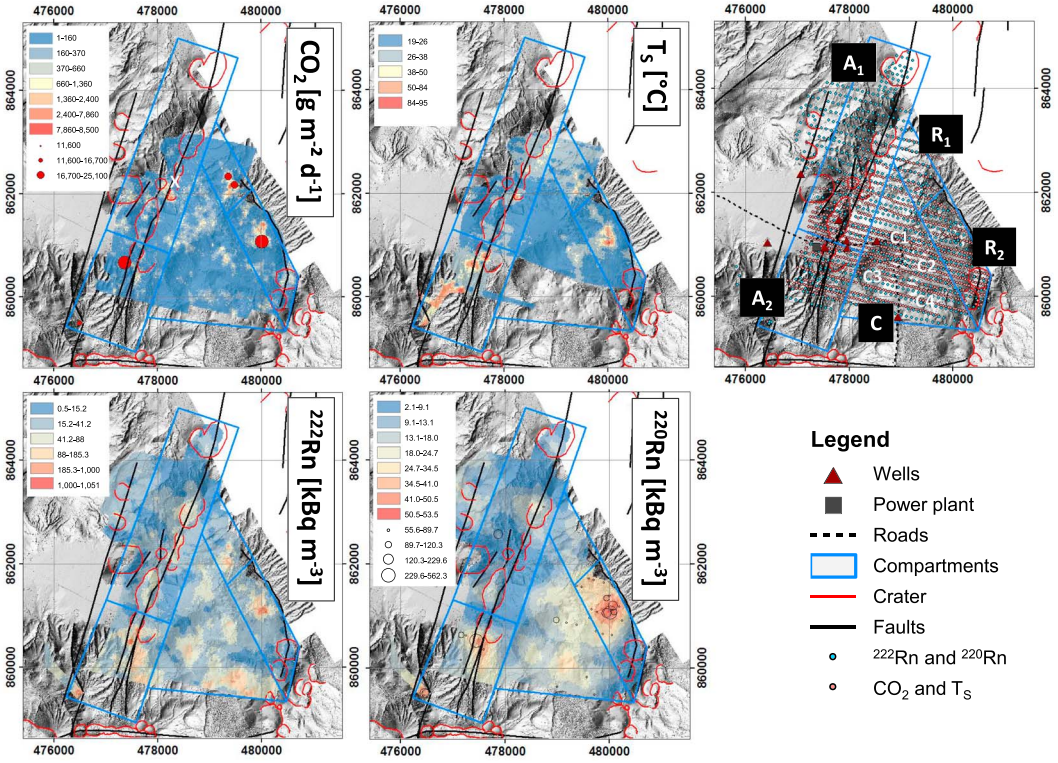

Figure 2. Interpolated maps for CO_2, T_S, ^{222}Rn, and ^{220}Rn. CO_2 values >8,500 g·m^{-2}·day^{-1} and ^{220}Rn values >53.5 kBq·m^{-3} are illustrated as points. Fault lines and craters have been digitized on the basis of a map from Kebede et al. (1985).

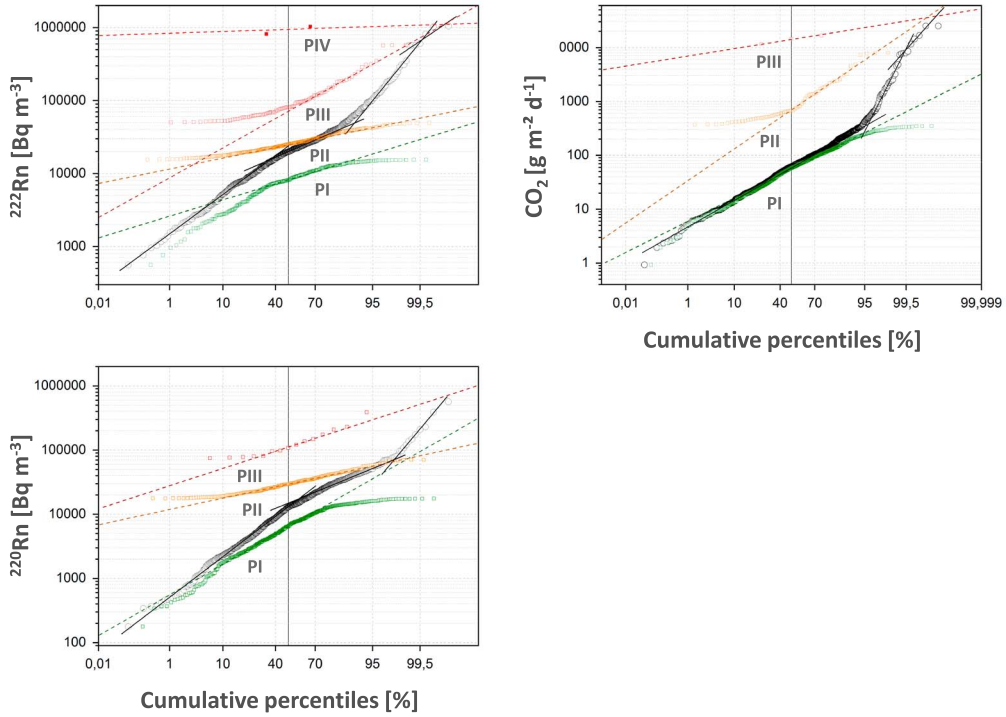

Figure 3. Probability plots for interpretation of the data. Following classification was introduced based on major inflection points in the probability plot of each dataset: CO_2 [g·m^{-2}·day^{-1}]: PI (Min–370), PII (370–8,500), PIII (8,500–Max); ^{222}Rn [kBq·m^{-3}]: PI (Min–15.5), PII (15.5–50.1), PIII (50.1–608.4), PIV (608.4–Max); ^{220}Rn [kBq·m^{-3}]: PI (Min–17.6), PII (17.6–71.8), PIII (71.8–Max).

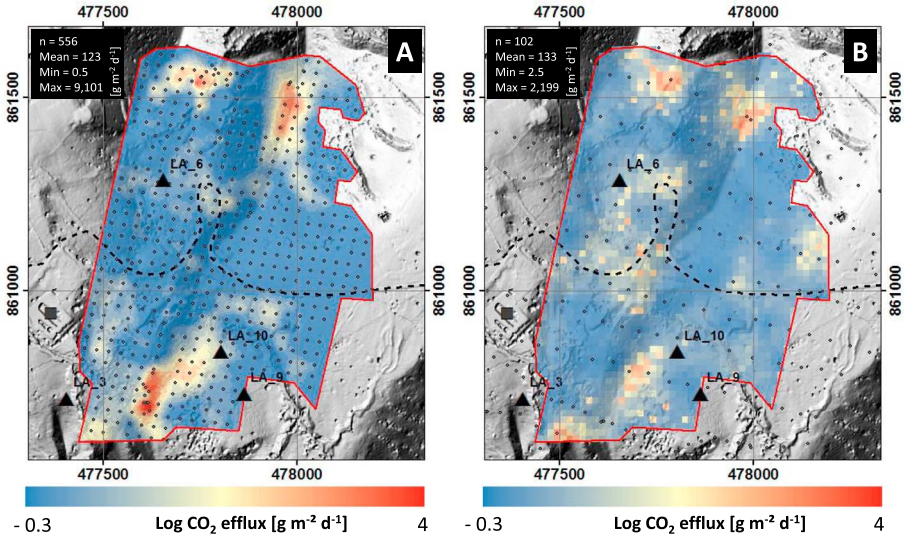

Figure 4. Detailed CO_2 efflux map from the transition zone A1 to A2 for the years 2012–2014 (a; from Hutchison et al., 2015, Hutchison, Biggs, et al., 2016) and 2016 (b). Stable degassing conditions at major degassing spots are indicated.

increased minimally. East of the intersection, slightly increased soil temperatures have been measured along a NNE-oriented zone. Anomalous ^{222}Rn values also appear beyond the intersection of the Ring Fault and AJFZ to the NNE in continuation of the AJFZ.

4.4. Thoron

The ^{220}Rn activity concentration dataset was separated into different classes based on major and minor inflection points in the probability plot (Figure 3). Additional class breaks have been defined for a finer discretization of the map (Figure 2). The majority of peak ^{220}Rn values (>71.8 kBq·m^{-3}) was measured at Bobesa. This anomaly extends to the West with decreasing values. Another peak ^{220}Rn cluster occurs in the Southern AJFZ and some medium ^{220}Rn values (17.6–71.8 kBq·m^{-3}) in Northern AJFZ. Activity concentration along Artu Jawe is increasing from the North toward the South. All values below 17.6 kBq·m^{-3} are considered as background.

4.5. Along Fault Variations

A profile of gas emissions along the AJFZ (X-X′; Figure 1) is shown in Figure 5. Fault-controlled emissions occur over a broad zone orthogonal to the fault (Figure 2), and so we filtered the emission data so that data within a fixed distance of the line were included in the plot (this is referred to as the buffer zone). For ^{222}Rn, ^{220}Rn, and T_S, a buffer zone of 500 m either side of the profile line was used, while for CO_2 a narrower buffer zone of 300 m was used. The narrower buffer zone for the CO_2 data was selected because data density is greater (as we included the high-spatial resolution survey of Hutchison et al., 2015; Figure 4). It is important to note that changing this buffer zone does not significantly affect the results and interpretations. We also calculated a running average (Figure 5, grey lines), by binning the data in 1 km segments along the fault so that we could identify whether there was any broad (kilometer-scale) change in emissions.

The along-fault plot (Figure 5) illustrates the trend of increasing gas emissions from the Northern AJFZ toward the Southern AJFZ. This correlating trend is reflected in all parameters (CO_2, ^{222}Rn, ^{220}Rn, and T_S). A possible explanation for this is the combination of volcanic (vicinity to a magmatic volatile source) and tectonic (structural permeability) impacts in Southern AJFZ, whereas the northern part of Artu Jawe is mainly tectonically influenced (permeable, but distant from magmatic volatile source). For both areas, gas emissions are highly variable over short (1–100 m) length scales, which can be explained by a fault segmentation, non-optimal orientation of the fracture zones in the acting stress field, sealing effects, and multiple upflow zones of geothermal fluids.

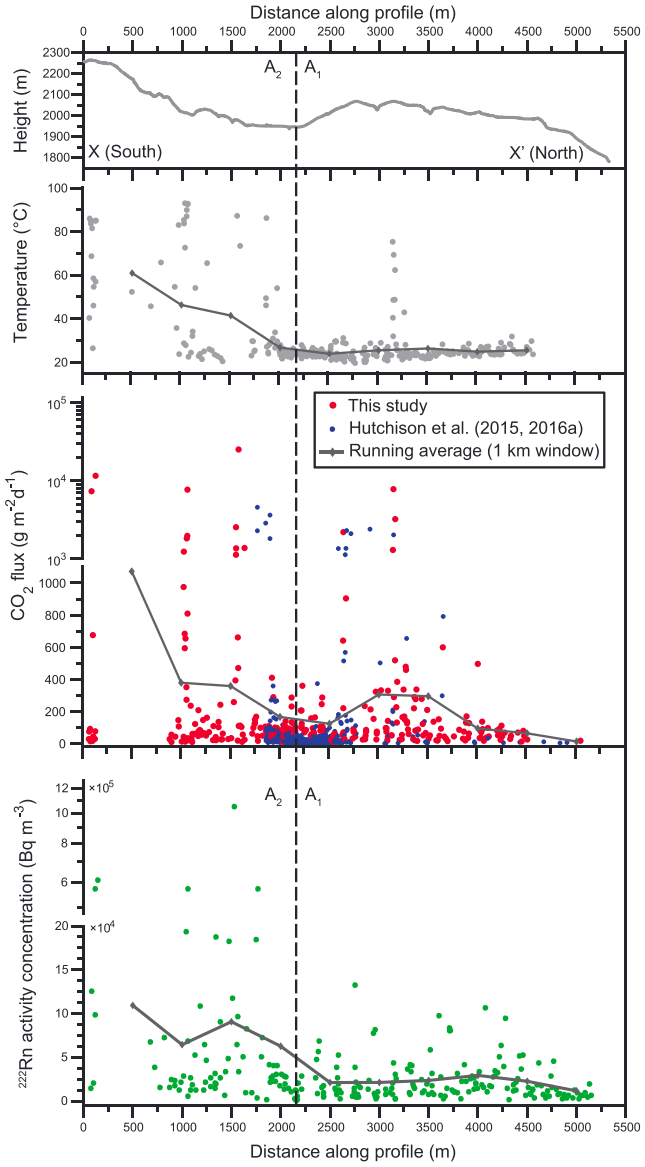

Figure 5. Along-fault variations of CO_2, ^{222}Rn, and soil temperature clearly show local peaks along the Artu Jawe Fault Zone and a general increase of gas release toward the South. The profile *X-X'* along the Artu Jawe Fault Zone is shown in Figure 1b. Fault-controlled emissions occur over a broad zone orthogonal to the fault (Figure 2). For that reason, data within a fixed distance orthogonal to the fault line was included in the plot (this is referred to as the buffer zone). We also calculated a running average by binning the data in 1 km segments along the fault to identify any broad (kilometer-scale) changes in emissions.

4.6. Soil Gas Fingerprint

A first attempt of a soil gas fingerprint analysis is presented in Figure 6. For each of the five analyzed key compartments (A1, A2, R1, R2, and C), a stacked column is plotted illustrating the maximum and mean values for ^{222}Rn, ^{220}Rn, CO_2 efflux, and T_S normalized to the maximum value in the entire study area. Such plots allow a fast spatial evaluation of the collected data. Here the significant differences in gas emissions originating from A2 and R2 versus A1, R1, and C can be recognized.

4.7. Radon-Thoron and Radon-Thoron-Carbon Dioxide Plots

Figure 7a reveals a tendency in all sectors toward increased RTRs (6.7–33) at different magnitudes for ^{222}Rn and ^{220}Rn (see also supporting information S1–S4). This indicates the presence of a significant hydrothermal upflow along permeable fracture zones from a deep source at medium fluid migration velocities. The main uranium and thorium source at Aluto is expected to be Neogene ignimbrites (below 1,400m depth), which are also hosting the geothermal reservoir where intense fluid-rock interaction occurs (Gizaw, 1993; Hutchison, Biggs, et al., 2016, Hutchison, Pyle, et al., 2016). Stratigraphic data from well logs show a uniform distribution of the ignimbrites across the study area (e.g., Teklemariam et al., 1996). Due to the lack of chemical information from well cuttings, data from analogue outcrops have been used to assess the chemical composition of the reservoir rocks. Analyses of rock samples from Aluto ignimbrites and basalts have shown that the ignimbrites are much richer in uranium and thorium than basalts (Ignimbrites: 10–20 ppm thorium and 2–4 ppm uranium; basalt: 2–5 ppm thorium; and 0–1 ppm uranium; Hutchison, Pyle, et al., 2016; Teklemariam, 1996). RTRs from 1.5 to 3.9 indicate a major hydrothermal upflow from a deep source and maximum fluid migration velocities. These ratios have been identified only in A2 and R2. Lower ^{222}Rn and ^{220}Rn magnitudes in A1 and R1, but peak RTRs, are interpreted as dilution effects. Whereas A1, R1, and R2 indicate the presence of deep and shallow sources, no shallow source is indicated for A2, which highlights the presence of a major hydrothermal upflow from a deep source. Selected maximum ^{222}Rn and ^{220}Rn values (^{222}Rn > 149.6 kBq·m^{-3}; ^{220}Rn > 80.7 kBq·m^{-3}) with a trend toward a deep source and maximum fluid migration velocities (RTR 1.5–3.9) are highlighted on the map (Figure 8) and illustrate major upflows from a deep source along the Southern AJFZ (A2) and the Ring Fault (R2).

The interpretation of the interpolated maps suggests a correlation of maximum ^{222}Rn, ^{220}Rn, and CO_2 emissions in most of the geothermally active areas. Based on a ternary plot (Figure 7b), this obvious correlation was further analyzed. The principle of this concept is to identify sites with simultaneous peaks from all three parameters, even if the actual magnitudes are relatively low. As a novelty, even for areas characterized by low-intermediate gas emissions, signals from deeper sources could be identified with this approach as illustrated in Figure 7b. CO_2 efflux values were extracted from the interpolated map based on the ^{222}Rn-^{220}Rn sampling grid. This extraction procedure was necessary due to different sampling grids for the two methods. For ^{222}Rn and ^{220}Rn, inverse values are plotted, so that the peak values from all parameter plot in the same corner of the ternary plot. A cluster of data points from all compartments becomes obvious in the CO_2-corner of the ternary plot. These values (CO_2 > 84%) have been extracted (manual selection) and plotted on a map (Figure 8). Many of the selected data points are constrained to areas with major

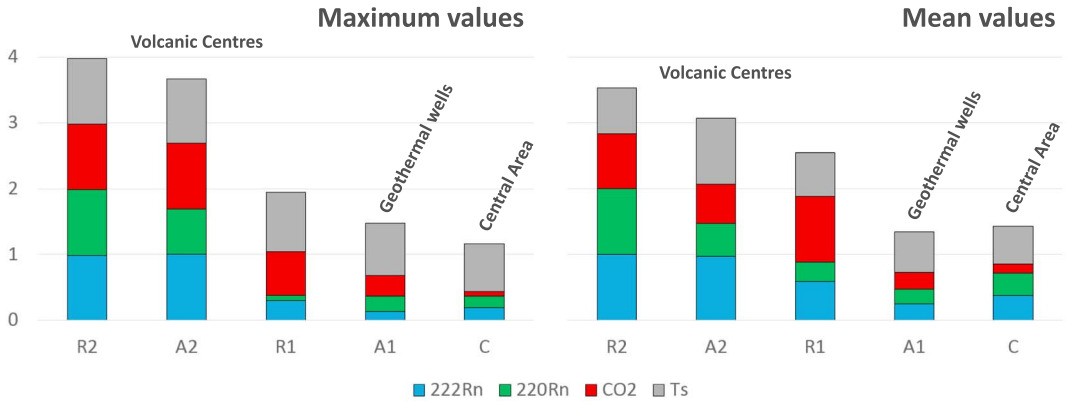

Figure 6. Soil gas fingerprint for the Northern and Southern Artu Jawe Fault Zone (A1 and A2), the Ring Fault (R1 and R2), and the Central Area (C) illustrated in a stacked bar chart for maximum and mean values. The compartment-specific maximum and mean values of each parameter have been normalized to the maximum value in the entire study area and are illustrated in a stacked bar chart. Example: In case the maximum values for each parameter have always been measured in the same compartment, the stacked column will have a value of 4.

geothermal anomalies. However, in addition to the well-known geothermal areas, this approach also highlights data points in the central part, which usually appeared less prominent and were therefore often considered as less important for structural permeability. Based on the ternary diagram, we found evidence for the existence of permeable structural pathways in the Central Area (Figures 7b and 8).

5. Discussion

5.1. Main Degassing Structures

In all investigated sectors, upflowing geothermal fluids are indicated (Figure 2). The pattern analysis of soil gas emissions implies (1) elongated upflows along permeable fracture segments and (2) locally concentrated upflows. Although Hutchison et al. (2015), Hutchison, Biggs, et al., (2016) identified the major structures, this new work clearly identifies and characterizes the major permeable structures, as well as the strong spatial variation of gas emissions.

5.1.1. Artu Jawe

The spatial pattern and variation of gas efflux and soil temperature suggest a strong fault segmentation with dextral displacements of Artu Jawe. Increased values of CO_2 efflux, ^{222}Rn, ^{220}Rn, and T_S have been observed along multiple well-confined NNE-oriented segments and within areas of maximum displacement, indicating major migration pathways of geothermal fluids. In the northern part of Artu Jawe, a significant dextral displacement of about 300 m creates permeability evidenced by increased CO_2 emissions (Figure 2; CO_2 map; marked as "X"). Maximum degassing rates occurred mainly within cluster of aligned

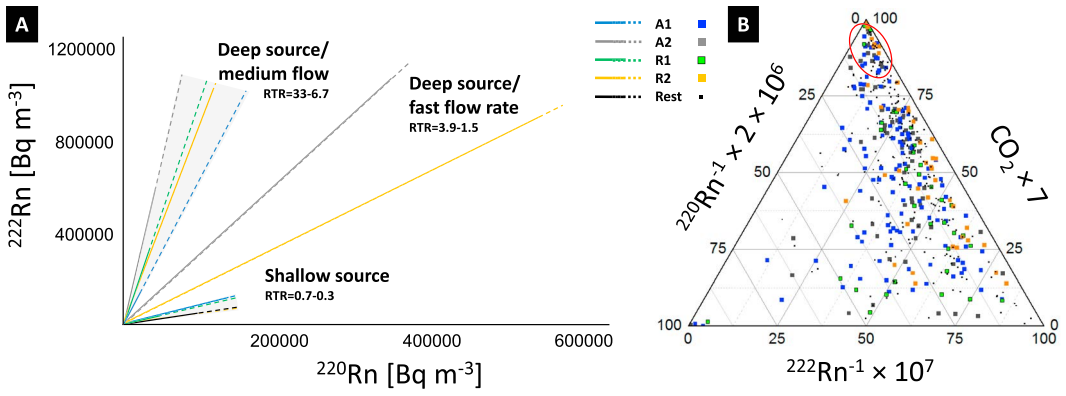

Figure 7. (a) ^{222}Rn versus ^{220}Rn plot for data from A1, A2, R1, R2, and Central Area (Rest) as depth indicator (see also supporting information S1–4); (b) ^{222}Rn-^{220}Rn-CO_2 ternary plot. The plot illustrates a cluster of data points with increased CO_2, ^{222}Rn, and ^{220}Rn values.

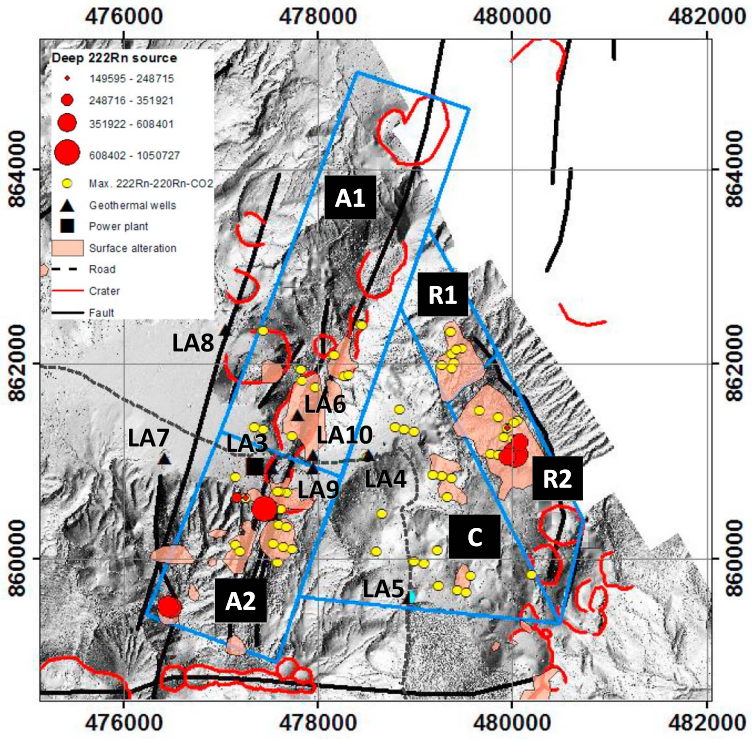

Figure 8. Sampling sites with coherent peak values for all three parameters have been extracted (from Figure 7b) and are shown on the map (yellow circles). Location of sampling sites with ^{222}Rn and ^{220}Rn values indicating a deep source and fast flow rates are illustrated as red circles (given as ^{222}Rn in Bq m^{-3}).

and elongated volcanic eruption craters, which have not been observed in the southern part of Artu Jawe (A2). Geothermal activity further North of the Aluto volcanic complex is decreasing. Peak CO_2 efflux and ^{222}Rn occurred in the Southern AJFZ, indicating a connection to the deep geothermal reservoir, but their spatial pattern appears to be less defined compared to the North. In contrast to the northern part, geothermal surface activity is indicated to continue Southward as can be seen by the presence of hot springs on the northern shore of Lake Langano in continuation of the structural trend of the AJFZ. Only minor surface alteration was observed in the North compared to the South. Less permeable segments could be affected by (1) silicic mineralization (sealing) of previously permeable fault segments (Teklemariam & Beyene, 2001) or (2) a nonpreferential fracture orientation in the acting stress field causing low structural permeability and hence less fluid circulation.

Along-fault variations on short length scales (100 m) and longer scales (kilometer; running average) are illustrated in Figure 5. Short length scale variations indicate fault segmentation and variable structural permeability, whereas long scale variations indicate regional trends, such as a general increase of gas emission to the South of AJFZ indicating a major source of magmatic volatiles.

The pattern of increased CO_2 efflux and ^{222}Rn values is not always congruent in the northern part of Artu Jawe. A possible explanation for this is the maturity of the geothermal manifestations. It is assumed that very young manifestations release mainly CO_2 in its initial phase. CO_2 from exsolution processes in magmatic sources travels to the surface once the magma is emplaced, for example, in dike intrusions. After some reaction time of hot and CO_2 bearing fluids with the reservoir rocks, more and more ^{222}Rn is released, which is ultimately resulting in a combination of increased ^{222}Rn and CO_2. Surface manifestations in its extinction phase seem to emit mainly ^{222}Rn and less CO_2. This could be explained by ongoing reaction processes of reservoir fluids and rocks, but an insufficient supply of new magmatic CO_2.

5.1.2. Ring Fault

CO_2 efflux, T_S, and ^{222}Rn anomalies have been detected in two key areas (Figure 2) on the western flank of the Ring Fault (Bobesa), but not on the rim itself. It is discussed if these surface manifestations should be

considered as solely Ring Fault related features (volcanic) or if they could have evolved as secondary features due to an interaction of the Ring Fault with additional (so far unknown) NNE-oriented tectonic structures (tectono-volcanic) parallel to the NNE-oriented AJFZ.

The area to the Southwest of the Ring Fault (C2) is characterized by widespread soil alteration, a large ^{220}Rn anomaly with decreasing values toward the West, and slightly increased T_S. This area seems to be largely affected by a geothermal outflow from Bobesa to the West. The source of the major degassing vents seems to be deep-rooted (Figure 2). Soil gas emissions show similar characteristics as A2.

At the inferred intersection of the Artu Jawe Fault and the Ring Fault, a nested eruption crater (~580 × 300 m) is located, where intermediate, but no maximum ^{222}Rn and ^{220}Rn values have been measured. CO_2 efflux values and T_S also do not show significantly higher values at the inferred intersection. In conclusion, observed gas emissions do not suggest an eminent permeability structure with a connection to a deep reservoir, although measured gas emissions are above background, indicating some minor fluid circulation.

5.1.3. Central Area

Magnitudes of gas emissions range from low to intermediate with a few peak values. Therefore, a hydrothermal system with similar characteristics as A2 or R2 is not expected in that area, though the presence of hydrothermal fluid circulation was proven with our approach. Wide-ranging CO_2 efflux (C1 and C2) and ^{222}Rn activity concentrations (C1–4) of low-intermediate magnitudes were identified in the Central Area (Figure 2). Geothermal surface activity was observed in C2 and C4. Increased CO_2 efflux in C1 can be interpreted as (1) a potential eastward directed shallow, lateral outflow from Artu Jawe (similar to a perched aquifer), and/or (2) increased structural permeability along an unknown NNE-oriented fracture zone. A biogenic source for these emissions is unlikely since biological sources (with isotopically light $\delta^{13}C$; Hutchison, Biggs, et al., 2016) show significantly lower fluxes and will not correlate with the high ^{222}Rn in the same area. Another rather small anomaly with increased CO_2 efflux and ^{222}Rn was identified in C2. Here increased T_S has been measured, and geothermal surface manifestations were observed. Possible explanations for this are as follows: (1) Presence of separate structure-controlled geothermal upflow, and/or (2) lateral outflow from Bobesa. An additional ^{222}Rn anomaly was detected in C3, which could be the result of another separate upflow of geothermal fluids along a NNE-oriented fault zone.

A large ^{222}Rn anomaly in the Southeast (C4) without obvious structural trends coincides with multiple, young volcanic eruption centers and lava flows. This area is also characterized by increased T_S, and CO_2 efflux, and seems to be an interesting target, worth more detailed investigation, as some data points show the same trends as observed in Aluto's high-temperature areas. The area has already been drilled (LA5, Figure 8), and data indicate the presence of an outflow zone at depth (Gizaw, 1993), which is probably due to its location at the boundary of the thermal anomaly. Further investigations could help to confirm or exclude the presence of a deep heat source. In general, NNE-oriented structures are indicated in the Central Area by the orientation of areas with increased gas emissions, but magnitudes are low and a very active hydrothermal system is not expected, though evidence of hydrothermal circulation is given. While we cannot rule out deep penetrating structures in this area, no significant fault scarps are observed at the surface.

5.2. Intersecting Faults

Hutchison et al. (2015) hypothesized that the intersection of the Ring Fault and AJFZ could be a spot of high magmatic gas efflux. However, the results from this study do not support a high magmatic gas efflux in this region. While there is a small increase in ^{222}Rn, ^{220}Rn, T_S, and CO_2 indicating a permeability structure, they do not confirm a connection to a deep source. The low gas flux at this intersection could be caused by a low permeability or limited fluids present at depth.

The two main areas on the Ring Fault with geothermal surface activity appear to coincide with fault intersections of the Ring Fault and additional NNE-oriented fault zones inferred based on increased gas emissions in the Central Area. These intersections may be important in controlling the upflow of deep fluids.

5.3. Implications for Geothermal Exploration

The observation of increased gas flux (in particular CO_2) along the AJFZ to the South is a good evidence for extra degassing by the presence of magma in the crust. Whether it is a mostly cooled plutonic body or large

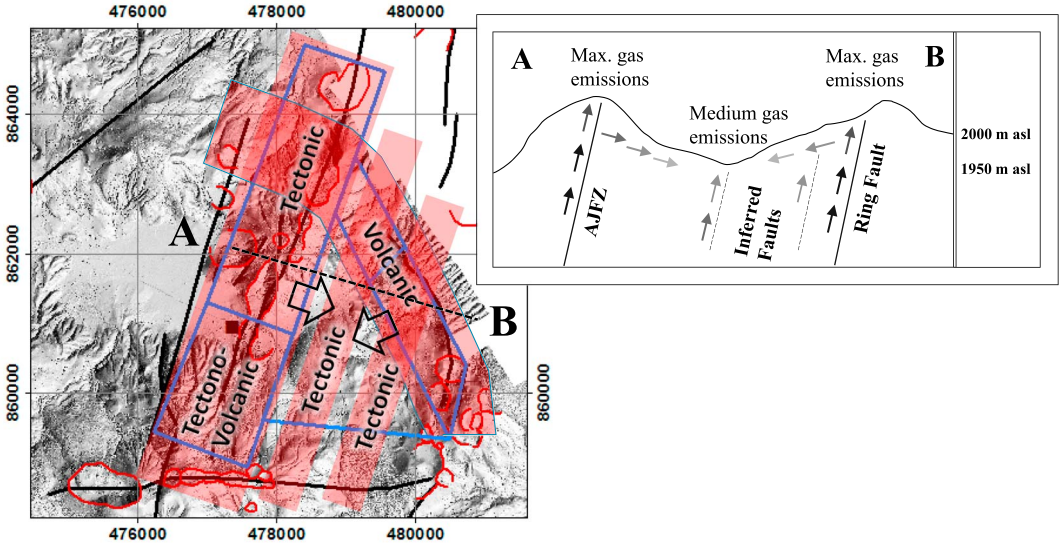

Figure 9. The developed conceptual model attempts to simplify the complex tectonic and volcanic setting of the Aluto Volcano. The Southern Artu Jawe Fault Zone is dominated by tectono-volcanic gas emissions. Along the Northern Artu Jawe Fault, the tectonic setting dominates surface gas emissions. The Ring Fault is a volcanic feature, which is likely to be affected by NNE-oriented structural features. Geothermal outflow zones are indicated by arrows.

body of melt is still unclear (Iddon et al., 2018), but the along fault plot seems like good evidence for a larger magmatic contribution than typically found along other faults in the rift (Hunt et al., 2017).

From a geothermal perspective, results clearly indicate increased fluid migration from a deep source along permeable fault structures in the southern part of the AJFZ (A2) and in the southeastern segment of the Ring Fault (R2). These areas are not yet targeted for geothermal exploitation but could be interesting prospects for future exploration and development as increased hydrothermal fluid circulation is expected and indicated by soil gas analysis. At this stage, only the northern part of the Artu Jawe Fault (A1) is exploited for geothermal power generation. The gas emissions in this sector point to a deep source as well but do not indicate an area of maximum hydrothermal fluid circulation due to lower gas emission rates compared to A2 or R2. The Southeastern part of the Central Area (C4) also reveals some degassing features with elevated gas efflux in an area with lots of young volcanic landforms. This implies the possibility of a contribution by fluids from a deep source and is worth further exploration efforts.

Generally, the gas emissions from Aluto are comparable to other geothermal systems in volcanic areas where diffuse degassing surveys have been performed for geothermal system analyses. A similar range of gas emissions was also observed in other fields (Giammanco et al., 2007; Jolie, Klinkmueller, et al., 2015). As a result of our area-wide measuring approach based on a predefined regular grid, we observe a limited number of peak values, and the majority of the data shows low values. This is different in comparison to other soil gas surveys, which usually focus on areas with the strongest gas efflux and obvious volcanic edifices (i.e., steam vents, hot pools, and surface alteration).

6. Conclusion

The Aluto volcanic complex is characterized by variable emission rates of volcanic gases and soil gas concentrations, which can be explained by its tectonic, volcanic, and tectono-volcanic setting. Apart from the two main structural features, that is, Artu Jawe Fault and Ring Fault, further sectors with increased gas emissions have been identified in between. Gas release along the Artu Jawe Fault reflects the general NNE-trend of the Wonji faults and is increasing from the tectonically dominated North toward the volcanic center in the South. This trend can be recognized for all investigated parameter. Similar results could be demonstrated in other geothermal fields in tectono-volcanic settings (e.g., Hernández et al., 2012). Significant differences in quantity of soil gas between A1 to A2 suggest a differentiation between a tectonic and tectono-volcanic compartment. The transition from the Northern to the Southern AJFZ in the vicinity of

the Aluto-Langano geothermal powerplant is a particularly interesting area, since outcropping segments of the Artu Jawe Fault are accessible without a cover of recent eruptive deposits (Hutchison et al., 2015). Here we observe a change from tectonic (North) to tectono-volcanic mode (South). The geothermal surface expressions at the Ring Fault are considered a result of volcanic and tectonic interactions (tectono-volcanic) and are similar to the southern part of the Artu Jawe Fault.

For a comprehensive and integrated interpretation of the identified gas emissions, a conceptual model was developed (Figure 9). The existence of two additional so far unknown NNE-oriented fracture zones in the Central Area is proposed. Available soil gas data support the hypothesis of their presence. This assumption is also supported by the ^{222}Rn-^{220}Rn-CO_2 plot, on which basis data points in the Central Area with maximum values were highlighted (Figure 8). Highlighted sampling sites suggest two NNE-oriented corridors of increased gas emissions. However, no obvious structural-geological evidence based on surface mapping was found. The presence of such structures could explain further geothermal surface expressions to the North and South of the study area (e.g., hot springs at northern shore of Lake Langano). They could also explain the two distinct geothermal areas along the Ring Fault as a result of intersecting NNE-oriented structures with the Ring Fault (volcano-tectonic origin). Based on this concept, we expect a continuation of areas with increased gas release toward the North and South as a result of rift-controlled degassing processes.

The results of the soil gas survey have a direct implication for future geothermal exploration and exploitation at the site, since it is indicated that exploration of the southern part of the AJFZ could also be prospective due to its combination of tectono-volcanic conditions (i.e., heat and structures). Further isotopic analyses (e.g., ^{3}He/^{4}He and d^{13}C) will help to better understand the source of the hydrothermal fluids and allow a direct comparison of Artu Jawe and Bobesa. In addition to the major geothermal areas, hydrothermal fluid circulation is also indicated in multiple areas in the central part, which is worth further investigations.

Acknowledgments
We thank all people from the Geological Survey of Ethiopia and our local field assistants, who helped to make the field work a great success. In particular, we thank Jonas Romrig and Bonso, who was an excellent field assistant. The project was financed in the framework of the Volkswagen Foundation's "Postdoctoral Fellowships for African Researchers in the Engineering Sciences" (reference: 90017). Data are accessible through the Research Data Repository of GFZ Data Services (dataservices.gfz-potsdam.de) or may be obtained from the author by reasonable request. The authors thank the reviewers of the paper for their constructive comments and suggestions.

References

Agostini, A., Bonini, M., Corti, G., Sani, F., & Manetti, P. (2011). Distribution of Quaternary deformation in the central Main Ethiopian Rift, East Africa. *Tectonics*, *30*, TC4010. https://doi.org/10.1029/2010TC002833

Bibby, H. M., Dawson, G. B., Rayner, H. H., Bennie, S. L., & Bromley, C. J. (1992). Electrical resistivity and magnetic investigations of the geothermal systems in the Rotorua area, New Zealand. *Geothermics*, *21*(1-2), 43–64. https://doi.org/10.1016/0375-6505(92)90067-J

Biggs, J., Bastow, I. D., Keir, D., & Lewi, E. (2011). Pulses of deformation reveal frequently recurring shallow magmatic activity beneath the Main Ethiopian Rift. *Geochemistry, Geophysics, Geosystems*, *12*, Q0AB10. https://doi.org/10.1029/2011GC003662

Boccaletti, M., Bonini, M., Mazzuoli, R., & Abebe, B. (1998). Quaternary oblique extensional tectonics in the Ethiopian Rift (Horn of Africa). *Tectonophysics*, *287*(1-4), 97–116. https://doi.org/10.1016/S0040-1951(98)80063-2

Braddock, M., Biggs, J., Watson, I. M., Hutchison, W., Pyle, D. M., & Mather, T. A. (2017). Satellite observations of fumarole activity at Aluto volcano, Ethiopia: Implications for geothermal monitoring and volcanic hazard. *Journal of Volcanology and Geothermal Research*, *341*, 70–83. https://doi.org/10.1016/j.jvolgeores.2017.05.006

Brune, S., Williams, S. E., & Müller, R. D. (2017). Potential links between continental rifting, CO_2 degassing and climate change through time. *Nature Geoscience*, *10*(12), 941–946. https://doi.org/10.1038/s41561-017-0003-6

Corti, G. (2009). Continental rift evolution: From rift initiation to incipient break-up in the Main Ethiopian Rift, East Africa. *Earth-Science Reviews*, *96*(1-2), 1–53. https://doi.org/10.1016/j.earscirev.2009.06.005

Darling, W. G., Gizaw, B., & Arusei, M. K. (1996). Lake-groundwater relationships and fluid-rock interaction in the East African Rift Valley: Isotopic evidence. *Journal of African Earth Sciences*, *22*(4), 423–431. https://doi.org/10.1016/0899-5362(96)00026-7

Di Paola, G. M. (1972). The Ethiopian Rift Valley (between 7° 00′ and 8° 40′ lat. North). *Bulletin of Volcanology*, *36*(4), 517–560. https://doi.org/10.1007/BF02599823

Ebinger, C. J., & Casey, M. (2001). Continental breakup in magmatic provinces: An Ethiopian example. *Geology*, *29*(6), 527–530. https://doi.org/10.1130/0091-7613(2001)029<0527:CBIMPA>2.0.CO;2

Fontijn, K., McNamara, K., Zafu Tadesse, A., Pyle, D. M., Dessalegn, F., Hutchison, W., et al. (2018). Contrasting styles of post-caldera volcanism along the Main Ethiopian Rift: Implications for contemporary volcanic hazards. *Journal of Volcanology and Geothermal Research*, *356*, 90–113. https://doi.org/10.1016/j.jvolgeores.2018.02.001

Fridriksson, T., Padrón, E., Óskarsson, F., & Pérez, N. M. (2016). Application of diffuse gas flux measurements and soil gas analysis to geothermal exploration and environmental monitoring: Example from the Reykjanes geothermal field, SW Iceland. *Renewable Energy*, *86*, 1295–1307. https://doi.org/10.1016/j.renene.2015.09.034

Gebregzabher, Z. (1986). Hydrothermal alteration minerals in Aluto Langano geothermal wells, Ethiopia. *Geothermics*, *15*(5-6), 735–740. https://doi.org/10.1016/0375-6505(86)90086-6

Giammanco, S., Sims, K. W., & Neri, M. (2007). Measurements of ^{220}Rn and ^{222}Rn and CO_2 emissions in soil and fumarole gases on Mt. Etna volcano (Italy): Implications for gas transport and shallow ground fracture. *Geochemistry, Geophysics, Geosystems*, *8*, Q10001. https://doi.org/10.1029/2007GC001644

Gianelli, G., & Teklemariam, M. (1993). Water-rock interaction processes in the Aluto-Langano geothermal field (Ethiopia). *Journal of Volcanology and Geothermal Research*, *56*(4), 429–445. https://doi.org/10.1016/0377-0273(93)90007-E

Gizaw, B. (1993). Aluto-Langano geothermal field, Ethiopian Rift Valley: Physical characteristics and the effects of gas on well performance. *Geothermics*, *22*(2), 101–116. https://doi.org/10.1016/0375-6505(93)90050-W

Goerner, A., Jolie, E., & Gloaguen, R. (2009). Non-climatic growth of the saline Lake Beseka, Main Ethiopian Rift. *Journal of Arid Environments*, *73*(3), 287–295. https://doi.org/10.1016/j.jaridenv.2008.09.015

Hernández, P. A., Pérez, N. M., Fridriksson, T., Jolie, E., Ilyinskaya, E., Thárhallsson, A., et al. (2012). Diffuse volcanic degassing and thermal energy release from Hengill volcanic system, Iceland. *Bulletin of Volcanology*, *74*(10), 2435–2448. https://doi.org/10.1007/s00445-012-0673-2

Hochstein, M. P., Oluma, B., & Hole, H. (2017). Geothermics early exploration of the Aluto geothermal field, Ethiopia (history of discovery well LA-3). *Geothermics*, *66*, 73–84. https://doi.org/10.1016/j.geothermics.2016.11.010

Hunt, J. A., Zafu, A., Mather, T. A., Pyle, D. M., & Barry, P. H. (2017). Spatially variable CO_2 degassing in the Main Ethiopian Rift: Implications for magma storage, volatile transport, and rift-related emissions. *Geochemistry, Geophysics, Geosystems*, *18*, 3714–3737. https://doi.org/10.1002/2017GC006975

Hutchison, W., Biggs, J., Mather, T. A., Pyle, D. M., Lewi, E., Yirgu, G., et al. (2016). Causes of unrest at silicic calderas in the East African Rift: New constraints from InSAR and soil-gas chemistry at Aluto volcano, Ethiopia. *Geochemistry, Geophysics, Geosystems*, *17*, 3008–3030. https://doi.org/10.1002/2016GC006395

Hutchison, W., Fusillo, R., Pyle, D. M., Mather, T. A., Blundy, J. D., Biggs, J., et al. (2016). A pulse of mid-Pleistocene rift volcanism in Ethiopia at the dawn of modern humans. *Nature Communications*, *7*(1), 13192. https://doi.org/10.1038/ncomms13192

Hutchison, W., Mather, T. A., Pyle, D. M., Biggs, J., & Yirgu, G. (2015). Structural controls on fluid pathways in an active rift system: A case study of the Aluto volcanic complex. *Geosphere*, *11*(3), 542–562. https://doi.org/10.1130/GES01119.1

Hutchison, W., Pyle, D. M., Mather, T. A., Yirgu, G., Biggs, J., Cohen, B. E., et al. (2016). The eruptive history and magmatic evolution of Aluto volcano: New insights into silicic peralkaline volcanism in the Ethiopian rift. *Journal of Volcanology and Geothermal Research*, *328*, 9–33. https://doi.org/10.1016/j.jvolgeores.2016.09.010

Iddon, F., Jackson, C., Hutchison, W., & Fontijn, K. (2018). Mixing and crystal scavenging in the Main Ethiopian Rift revealed by trace element systematics in feldspars and glasses. *Geochemistry, Geophysics, Geosystems*, *20*, 230–259. https://doi.org/10.1029/2018GC007836

Jolie, E., Klinkmueller, M., & Moeck, I. (2015). Diffuse surface emanations as indicator of structural permeability in fault-controlled geothermal systems. *Journal of Volcanology and Geothermal Research*, *290*, 97–113. https://doi.org/10.1016/j.jvolgeores.2014.11.003

Jolie, E., Klinkmueller, M., Moeck, I., & Bruhn, D. (2016). Linking gas fluxes at Earth's surface with fracture zones in an active geothermal field. *Geology*, *44*(3), 187–190. https://doi.org/10.1130/G37412.1

Jolie, E., Moeck, I., & Faulds, J. E. (2015). Quantitative structural-geological exploration of fault-controlled geothermal systems—A case study from the Basin-and-Range Province, Nevada (USA). *Geothermics*, *54*, 54–67. https://doi.org/10.1016/j.geothermics.2014.10.003

Kebede, S. (2012). Geothermal exploration and development in Ethiopia: Status and future plan. Short Course VII Exploration of Geothermal Resources.

Kebede, S., Mamo, T., & Abebe, T. (1985). Geological report and explanation to the geological map of Aluto-Langano geothermal area. Addis Ababa, Ethiopian Institute of Geological Surveys, 60 p.

Keir, D., Bastow, I. D., Corti, G., Mazzarini, F., & Rooney, T. O. (2015). The origin of along-rift variations in faulting and magmatism in the Ethiopian Rift. *Tectonics*, *34*, 464–477. https://doi.org/10.1002/2014TC003698

Lee, H., Muirhead, J. D., Fischer, T. P., Ebinger, C. J., Kattenhorn, S. A., Sharp, Z. D., & Kianji, G. (2016). Massive and prolonged deep carbon emissions associated with continental rifting. *Nature Geoscience*, *9*(2), 145–149. https://doi.org/10.1038/ngeo2622

Lloyd, R., Biggs, J., Wilks, M., Nowacki, A., Kendall, J., Ayele, A., et al. (2018). Evidence for cross rift structural controls on deformation and seismicity at a continental rift caldera. *Earth and Planetary Science Letters*, *487*, 190–200. https://doi.org/10.1016/j.epsl.2018.01.037

Maguire, P. K. H., Keller, G. R., Klemperer, S. L., Mackenzie, G. D., Keranen, K., Harder, S., et al. (2006). Crustal structure of the northern Main Ethiopian Rift from the EAGLE controlled-source survey; A snapshot of incipient lithospheric break-up. *Geological Society of London, Special Publication*, *259*(1), 269–292. https://doi.org/10.1144/GSL.SP.2006.259.01.21

Mohr, P. A. (1967). Major volcano-tectonic lineament in the Ethiopian Rift System. *Nature*, *213*(5077), 664–665. https://doi.org/10.1038/213664a0

Molin, P., & Corti, G. (2015). Tectonophysics topography, river network and recent fault activity at the margins of the Central Main Ethiopian Rift (East Africa). *Tectonophysics*, *664*, 67–82. https://doi.org/10.1016/j.tecto.2015.08.045

Neri, M., Ferrera, E., Giammanco, S., Currenti, G., Cirrincione, R., Patanè, G., & Zanon, V. (2016). Soil radon measurements as a potential tracer of tectonic and volcanic activity. *Scientific Reports*, *6*(1), 24581. https://doi.org/10.1038/srep24581

Nowacki, A., Wilks, M., Kendall, J., Biggs, J., & Ayele, A. (2018). Characterising hydrothermal fluid pathways beneath Aluto volcano, Main Ethiopian Rift, using shear wave splitting. *Journal of Volcanology and Geothermal Research*, *356*, 331–341. https://doi.org/10.1016/j.jvolgeores.2018.03.023

Rango, T., Petrini, R., Stenni, B., Bianchini, G., Slejko, F., Beccaluva, L., & Ayenew, T. (2010). The dynamics of central Main Ethiopian Rift waters: Evidence from δD, $\delta^{18}O$ and $^{87}Sr/^{86}Sr$ ratios. *Applied Geochemistry*, *25*, 1860–1871. https://doi.org/10.1016/j.apgeochem.2010.10.001

Saibi, H., Aboud, E., & Ehara, S. (2012). Analysis and interpretation of gravity data from the Aluto-Langano geothermal field of Ethiopia. *Acta Geophysica*, *60*(2), 318–336. https://doi.org/10.2478/s11600-011-0061-x

Samrock, F., Grayver, A. V., Eysteinsson, H., & Saar, M. O. (2018). Magnetotelluric image of transcrustal magmatic system beneath the Tulu Moye geothermal prospect in the Ethiopian Rift. *Geophysical Research Letters*, *45*, 12–847. https://doi.org/10.1029/2018GL080333

Samrock, F., Kuvshinov, A., Bakker, J., Jackson, A., & Fisseha, S. (2015). 3-D analysis and interpretation of magnetotelluric data from the Aluto-Langano geothermal field, Ethiopia. *Geophysical Journal International*, *202*(3), 1923–1948. https://doi.org/10.1093/gji/ggv270

Saria, E., Calais, E., Stamps, D. S., Delvaux, D., & Hartnady, C. J. H. (2014). Present-day kinematics of the East African Rift. *Journal of Geophysical Research: Solid Earth*, *119*, 3584–3600. https://doi.org/10.1002/2013JB010901

Siebert, L., & Simkin, T. (2002). Volcanoes of the world: An illustrated catalog of Holocene volcanoes and their eruptions: Smithsonian Institution, Global Volcanism Program Digital Information Series, GVP-3 (www.volcano.si.edu/gvp/world/).

Teklemariam, M. (1996). Water-rock interaction processes in the Aluto-Langano geothermal field Ethiopia. Unpublished Ph. D Thesis, University of Pisa, 245 pp. University of Pisa.

Teklemariam, M., Battaglia, S., Gianelli, G., & Ruggieri, G. (1996). Hydrothermal alteration in the Aluto-Langano geothermal field, Ethiopia. *Geothermics*, *25*(6), 679–702. https://doi.org/10.1016/S0375-6505(96)00019-3

Teklemariam, M., & Beyene, K. (2001). Geochemical monitoring of the Aluto-Langano geothermal field, Ethiopia. Proceedings Stanford Geothermal Workshop.

Valori, A. M., Teklemariam, M., & Ginaelli, G. (1992). Evidence of temperature increase of CO_2-bearing fluids from Aluto-Langano geothermal field (Ethiopia): A fluid inclusions study of deep wells LA-3 and LA-6. *European Journal of Mineralogy*, *4*(5), 907–920. https://doi.org/10.1127/ejm/4/5/0907

WEST Systems, 2019. Carbon dioxide flux meter, Handbook, Release 9.1, January 2019, URL: https://www.westsystems.com/wp-content/uploads/2019/01/Handbook_Portable_9.1.pdf (Retrieved May 17th, 2019).

Wilks, M., Kendall, J., Nowacki, A., Biggs, J., Wookey, J., Birhanu, Y., et al. (2017). Seismicity associated with magmatism, faulting and hydrothermal circulation at Aluto Volcano, Main Ethiopian Rift. *Journal of Volcanology and Geothermal Research*, *340*, 52–67. https://doi.org/10.1016/j.jvolgeores.2017.04.003

Younger, P. L. (2014). Missing a trick in geothermal exploration. *Nature Geoscience*, *7*(7), 479–480. https://doi.org/10.1038/ngeo2193